Nanoscale Research Letters

NANO EXPRESS Open Access

Dynamic Control of High-Range Photoresponsivity in a Graphene Nanoribbon Photodetector

Juan Yu[1,2*†], Jiahong Zhong[2†], Xiaofei Kuang[1†], Cheng Zeng[2], Lingkai Cao[2], Yanping Liu[2,3,4*] and Zongwen Liu[5*]

Abstract

Graphene has been demonstrated to be a promising material for optoelectronics and photodetection devices because of its ultra-broadband optical absorption and high carrier mobility. However, its integration with optoelectronic systems has been limited by the zero-bandgap and the lack of a gain mechanism. Herein, we demonstrate a novel photodetector based on the graphene nanoribbons (GRNs) with a sizable bandgap. Utilizing trapping charge at the interface between SiO_2 and light-doped silicon, an ultrahigh gain of 22,400 has been obtained. Our devices show an enhanced photoresponsivity (~ 800 AW^{-1}) while the response speed is still fast (up to 10 μs). This photoresponsivity is about two orders of magnitude higher compared to that of a previous graphene-based photodetector. The photodetector exhibits a wide-range tunability via source-drain bias and back gate voltage. Our work addresses key challenges for the photodetectors and potentially provides the desired pathway toward practical application of graphene photodetectors that can be externally manipulated by an electric field with fast response speed and high sensitivity.

Keywords: Graphene nanoribbons, Photodetector, Photoresponsivity

Introduction

Graphene, a two-dimensional (2D) layered material, plays an important role in many fields including electrodialysis [1], batteries [2], nanofiltration [3], catalysis [4], electromagnetic interference [5], and optoelectronics. Significantly, graphene has attracted much attention owing to its novel optoelectronic properties [6–9], such as high carrier mobility [10, 11], zero-bandgap [12–14], and tunable Fermi level [15]. Therefore, graphene has been considered as an attractive material for optoelectronic applications [16–18]. However, the low absorption (~ 2.3%) of the monolayer graphene resulting from its thin thickness is still a critical challenge [19]. On the other hand, its zero-bandgap characteristic severely limits the optoelectronic applications, which causes a short photo-generated carrier lifetime (~ps) and results in the fast electron-hole recombination [20, 21]. As a consequence, further improvement of the responsivity of the pristine graphene photodetector remains challenging, and it is of considerable significance to separate the electrons and holes to generate an efficient photocurrent.

To overcome these challenges, various techniques have been explored and the photoresponsivity of photodetectors based on graphene has been enhanced accordingly. Photogating effect [22], which is usually observed in photodetectors based on low-dimensional materials and their hybrid structures, plays an essential role in the high performance of photodetectors. Photodetectors based on $MoTe_2$ [23] and MoS_2 [24] using the photogating effect have been reported, and photodetectors with excellent

* Correspondence: juanyu@hdu.edu.cn; liuyanping@csu.edu.cn; zongwen.liu@sydney.edu.au
†Juan Yu, Jiahong Zhong and Xiaofei Kuang contributed equally to this work.
[1]School of Electronics and Information, Hangzhou Dianzi University, 1158 Second Street, Xiasha College Park, Hangzhou 310018, Zhejiang, People's Republic of China
[2]School of Physics and Electronics, Hunan Key Laboratory for Super-microstructure and Ultrafast Process, Central South University, 932 South Lushan Road, Changsha, Hunan 410083, People's Republic of China
[5]School of Chemical and Biomolecular Engineering, The University of Sydney, Camperdown, Sydney, NSW 2006, Australia
Full list of author information is available at the end of the article

performance based on graphene utilizing photogating effect have also been achieved. It was demonstrated that combining graphene and PbS quantum dots was an effective way to enhance the absorption of light and achieve an ultrahigh gain in a graphene photodetector [25]. Besides, the recombination of electrons and holes could also be minimized in a photodetector based on heterostructures, such as graphene-Ta_2O_5-graphene [26], where the photoinduced electron-hole pairs were separated via quantum tunneling effects, leading to the great enhancement of the photoresponsivity and the gain. The response time of such hybrid-structure photodetector was seriously increased resulting from the long trapping time of the carriers in the PbS quantum dots or in the Ta_2O_5 tunnel barrier. Thus, it is highgly demanded for the graphene-based photodetector to achieve excellent performances in responsivity, response time, and spectral response.

Here, we propose a photodetector based on 20-nm-wide graphene nanoribbons and demonstrate its photoresponsivity (up to 800 AW^{-1}) and fast response speed (~ 10 μs). Such high performance is mainly attributed to the sizable bandgap in the GNRs, enhanced by the photogating effect at the silicon/silicon oxide (Si/SiO_2) interface. The physical mechanism of the detector was explained by the energy band diagrams. Furthermore, the photodetector based on GNRs can be tuned by source-drain and back-gate voltage. The observed high performance substantially paves the way for developing high-responsivity and ultrafast graphene photodetectors.

Experimental Methods

The graphene sheet was exfoliated onto a Si substrate (covered with 300 nm SiO_2) from the graphite bulk (grade ZYA, SPI Supplies) by the 3M-tape micromechanical cleavage technique. Graphene nanoribbons with a width of 20 nm were fabricated using reactive-ion etching (RIE, PE-3A) and electron beam lithography (EBL, Raith BV EBPG5150). After this, the monolayer graphene and graphene nanoribbon on the SiO_2 dielectric were characterized by an optical microscope and Raman spectroscopy (WITec Alpha 300R). Standard photolithography and e-beam evaporation of Ti/Au (20 nm/80 nm) were used to create the source and drain electrodes. Eight devices (16 GNRs) were fabricated, and 5 of them possess excellent performance. All the measurements were carried out through a home-made system composed of a laser light source, an optical chopper, a 4-probe stage, and a semiconductor parameter analyzer. A lower doped silicon (P-type 10–20 Ω cm) substrate was used to enhance the photogating effect. A Ti:Sapphire visible laser at a wavelength of around 632 nm was employed to generate laser pulses within an area of 6.25 mm^2 at room temperature. The frequency of the incident light was modulated with an optical chopper in a range from 5 Hz to 50000 Hz. Besides, incident laser power could be adjusted from 0.34 mW to 5 mW. The data shown in the figures, including current (Figs. 1c, d, 2a–d, 3a, b, 4a–d, and 5a, b), was obtained from a semiconductor parameter analyzer (Agilent, B1500A) with or without illumination. All the photoresponse measurements were carried under ambient conditions.

Results and Discussion

GNRs are expected to be an ideal carrier for photodetection. The GNR photodetector that we fabricated was comprised of the source and the drain electrodes on a Si/SiO_2 substrate with a lightly doped silicon wafer acting as a back gate, as shown schematically in Fig. 1a. To ensure the high mobility and obtain a large enough bandgap simultaneously, the width of the graphene nanoribbons was chosen to be a moderate 20 nm. The complete structure of the GNRs is shown in the scanning electron microscope image (Fig. 1b), and the length of the graphene nanoribbons was 2 μm. Different from the conventional photodetectors, the lightly doped Si was adopted as the substrate for the reason that its carrier lifetime is much longer than that in the heavily doped Si [27].

The electrical characterization was repeatedly carried out and the consequent I-V_{S-D} relationship is plotted in Fig. 1c. The curves under different back-gate voltages in a range from − 10 V to 10 V are nonlinear and asymmetric, indicating the existence of the internal electric field, which might be resulted from the fabrication-induced defects or the Schottky barrier at the electrodes contacts. The internal electric field had a nonnegligible effect on the photocurrent of the GNR photodetector, which will be illustrated later. The inset is the comparison of I-V characteristics of the device under dark and illumination (applying a laser pulse with a frequency of 10 Hz), manifesting the sensitive optical-switching tunability. Obviously, the I-V curve shifted as the V_G varied. To further figure out the effect of V_G on the charge transport characteristics of the GNR channel, the transfer characteristics in the dark state were recorded at room temperature as shown in Fig. 1d. The measured $I_D - V_G$ curve at V_{SD} = 10 mV demonstrated that our device displayed a typical behavior of the graphene-based photodetector, and the GNRs acted as a p-type channel with a shift of 20 V.

For typical optoelectronic systems, the response speed (characterized by the total time required for the output to rise (fall) from 10 (90)% to 90 (10)% of the pulse peak) of a photodetector determines the running speed and information capacity of the photodetection system. To investigate the ultimate response time of the fabricated device, the input optical signal with different pulse

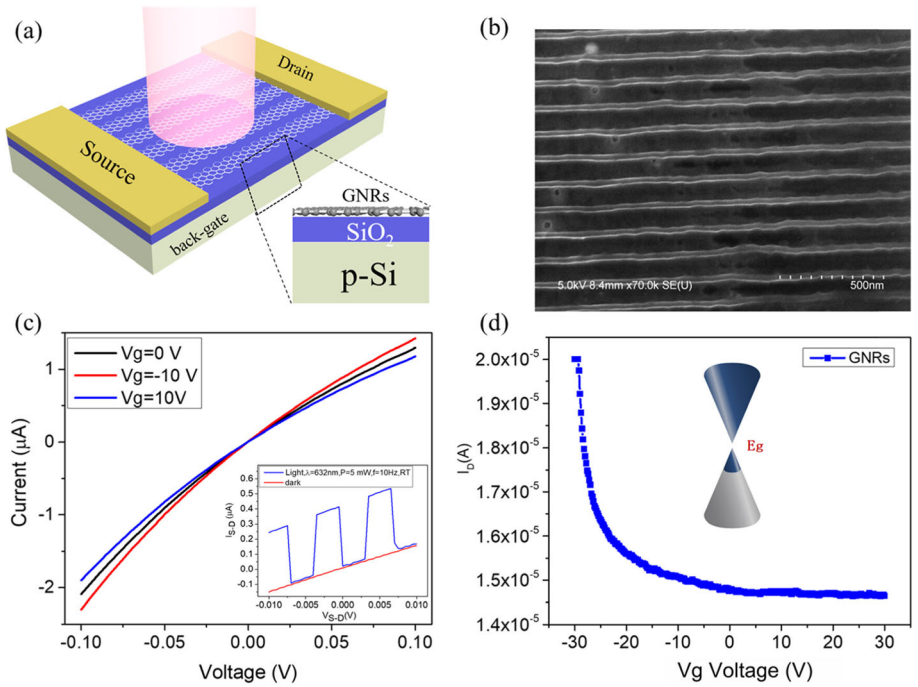

Fig. 1 **a** A schematic illustration of the GRN photodetector. It is similar to the FET device comprised of the source and the drain electrode on the Si/SiO_2 substrate with a lightly doped Si wafer acting as a back gate. The incident light was modulated by an optical chopper of variable frequency. **b** SEM image of the GRN photodetector device. **c** Current-voltage (I-V) characteristics of the GRN device under different back-gate voltage. Inset: I-V characteristics of the device under dark (red line) or illumination with a frequency of 10 Hz (blue line). **d** The source-drain current versus the back-gate voltage bias of GNR photodetector at room temperature. Inset: schematic diagram of GNR band structure

frequencies of 40 Hz, 400 Hz, and 50,000 Hz were applied. Fig. 2b–d show the corresponding time-resolved total photocurrents, which intuitively reflect that the fabricated photodetector could be efficiently switched on and off with excellent repeatability. Furthermore, when the laser frequency was adjusted to 50,000 Hz, the rising time was measured to be 10 μs. We believe that our device is expected to operate at higher frequencies over 50,000 Hz, and the accurate value of response speed is not clear due to the limitation of the measuring equipment. It was noted that the GNR photodetector run much faster than most photodetectors based on graphene and other 2D TMDs [28–31]. It is believed that the fast photocurrent switching can be attributed to the ultra-high carrier mobility of the GNRs of such width and the strong external electric field.

In addition to the fast response speed, high responsivity and enhanced gain are indispensable for the application of the photodetector. Therefore, through applying light on the entire device at room temperature, we further studied the photoresponse of the GNR photodetector without source-drain bias and back-gate voltage. Figure 2a presents the time-dependent photocurrent measurements of the device in the absence of the biased voltage under on-off light modulation. The observed photocurrent was 275 nA($I_{\text{illumination}}$ = 293 nA, I_{dark} = 18 nA) under illumination, which indicated a high photoresponsivity of R = 17.2 AW^{-1} and a high gain of G = 1465 as well, calculated via the following two equations:

$$R = \frac{I_P}{\frac{S_G}{S_L} \cdot P} \tag{1}$$

$$G = \frac{I_P/e}{\left(\frac{S_G}{S_L} \cdot P \cdot 2.3\%\right)/h\nu} \left(\nu = \frac{c}{\lambda_{in}}\right) \tag{2}$$

where I_P (275 nA) is the photocurrent, while S_L (6.25 mm^2) and S_G (2 μm×10 μm) are the actual area of the laser and the GNR, respectively, and P (5 mW) is the power of incident laser with a wavelength of λ_{in} (532 nm). It is essential to explore the photocurrent generation mechanism of the GNR photodetectors to clarify the high performance of our devices. For photodetectors based on two-dimensional materials, there are mainly two photocurrent generation mechanisms: the photoconductive effect (PC) and the photovoltaic effect (PV) [32].

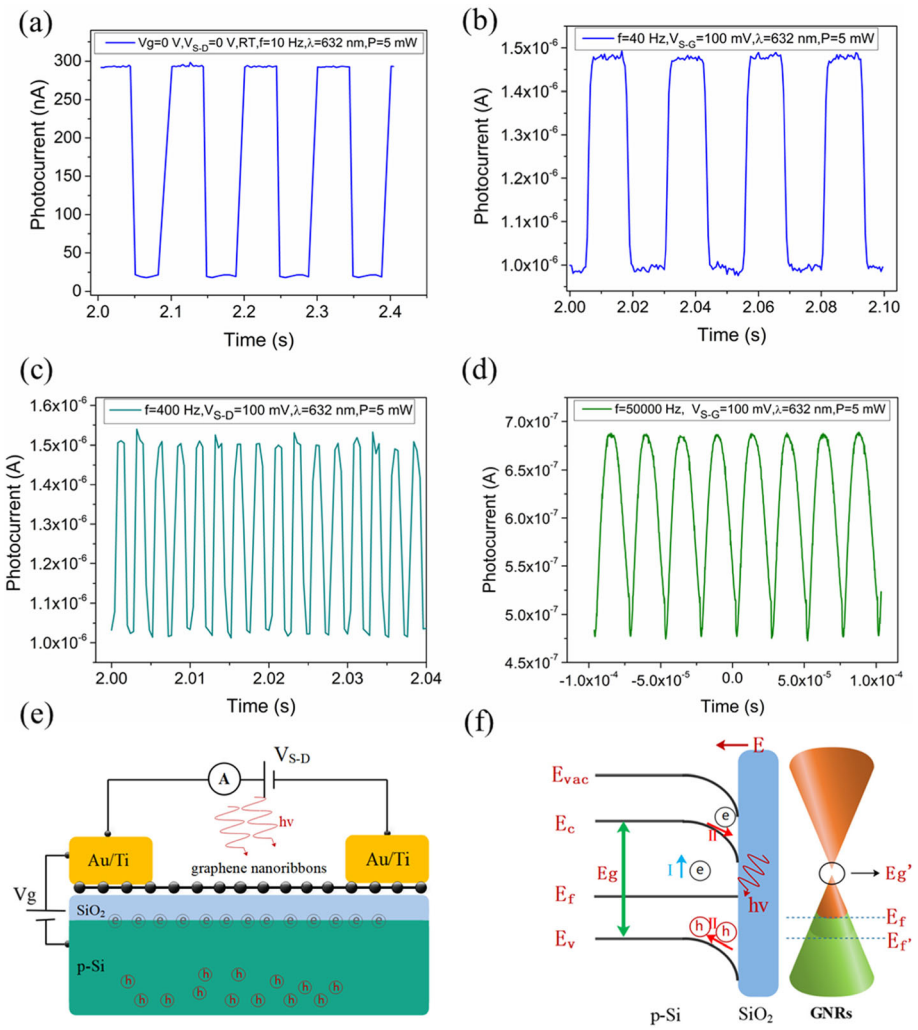

Fig. 2 **a** Time-dependent photocurrent measurements of the device without the biased of back-gate and source-drain voltage under on-off light (632 nm) modulation at room temperature. The time-dependence photocurrent was measured under laser illumination with a frequency of 40 Hz (**b**), 400 Hz (**c**), and 5000 Hz (**d**). **e** Schematic diagram of the GNR photodetector. **f** Energy diagram of the interface between Si and SiO_2 upon light illumination. E_C, E_V, E_{fs}, and E_{VAC} are the conduction band, valence band, Fermi level, and vacuum level, respectively. E_f and E_f' are the Fermi level before and after the injection of the electron to the GNR channel. E_g' is the bandgap of GNRs. Two processes are illustrated: (I) electronic transition from the value band to the conduction band under illumination in Si and SiO_2; (II) hole transfer from SiO_2 to Si and photon excited carriers drifted through the built-in field

Without applying a source-drain bias, PV was responsible for the photocurrent generation as the two built-in electrical fields were formed between the GNRs and the electrodes. The two electrical fields were not the same magnitude due to defects formed in the manufacturing process. When the light reached the region at the Au-GNRs interface, the photo-generated electron-hole pairs were generated and subsequently separated by the built-in fields, which made a significant contribution to the photocurrent generation. Under a source-drain bias, however, the two built-in electrical fields at the Au-GNRs interface played little part in photocurrent generation. Therefore, PC played the most crucial role in the photocurrent generation in the case of applying a source-drain bias. After absorbing photons, the GNR channel generated more free carriers, reducing the resistance of the carrier channels. Therefore, a significant photocurrent $I_P = \frac{V_{OC}}{R_G}$ (V_{OC} represents the open-circuit voltage and R_G is the total resistance of the channel formed by the 16 graphene nanoribbons) was observed.

As can be seen in Fig. 2a–d, a μA-level photocurrent was observed, which might be due to the contribution of three aspects. One was that the electron-hole pair recombination rate was reduced resulting from the bandgap in the GNRs. The other was that the photogenerated

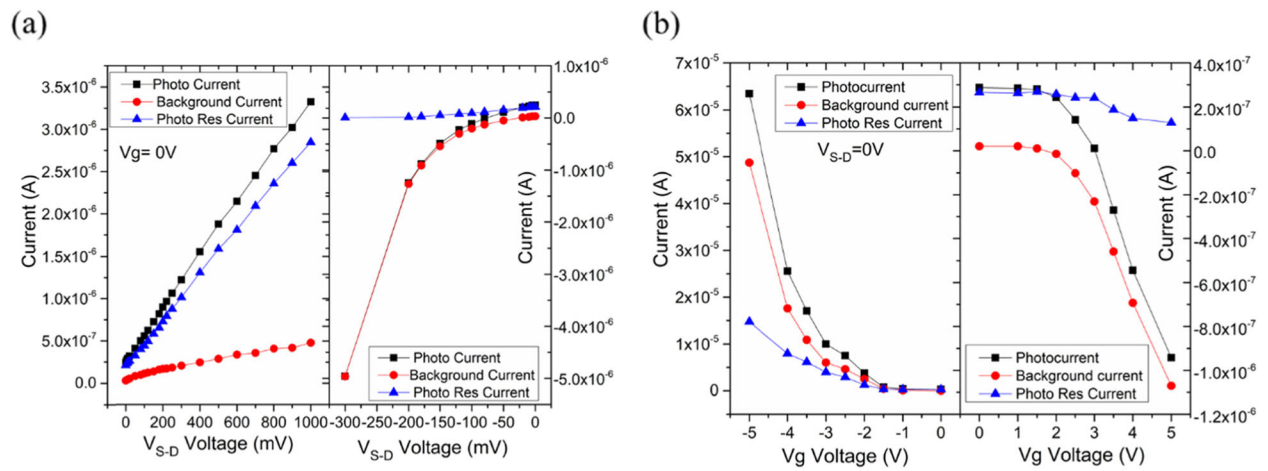

Fig. 3 **a** Photocurrent dependence on the biased source-drain voltage. Photocurrent, background current, and photoresponse current measurements of GRN photodetector in biased of back-gate voltage. The decrease of the photocurrent with an increase of the biased source-drain voltage was contributed to the improvement of the separation efficiency of photo-generated electron-hole pairs. **b** Photocurrent dependence on the back-gate voltage. The biased back-gate voltage dependence of the photocurrent characteristics in biased of source-drain voltage. The results indicate that the photocurrent could be modulated via biasing the source-drain voltage and gate voltage

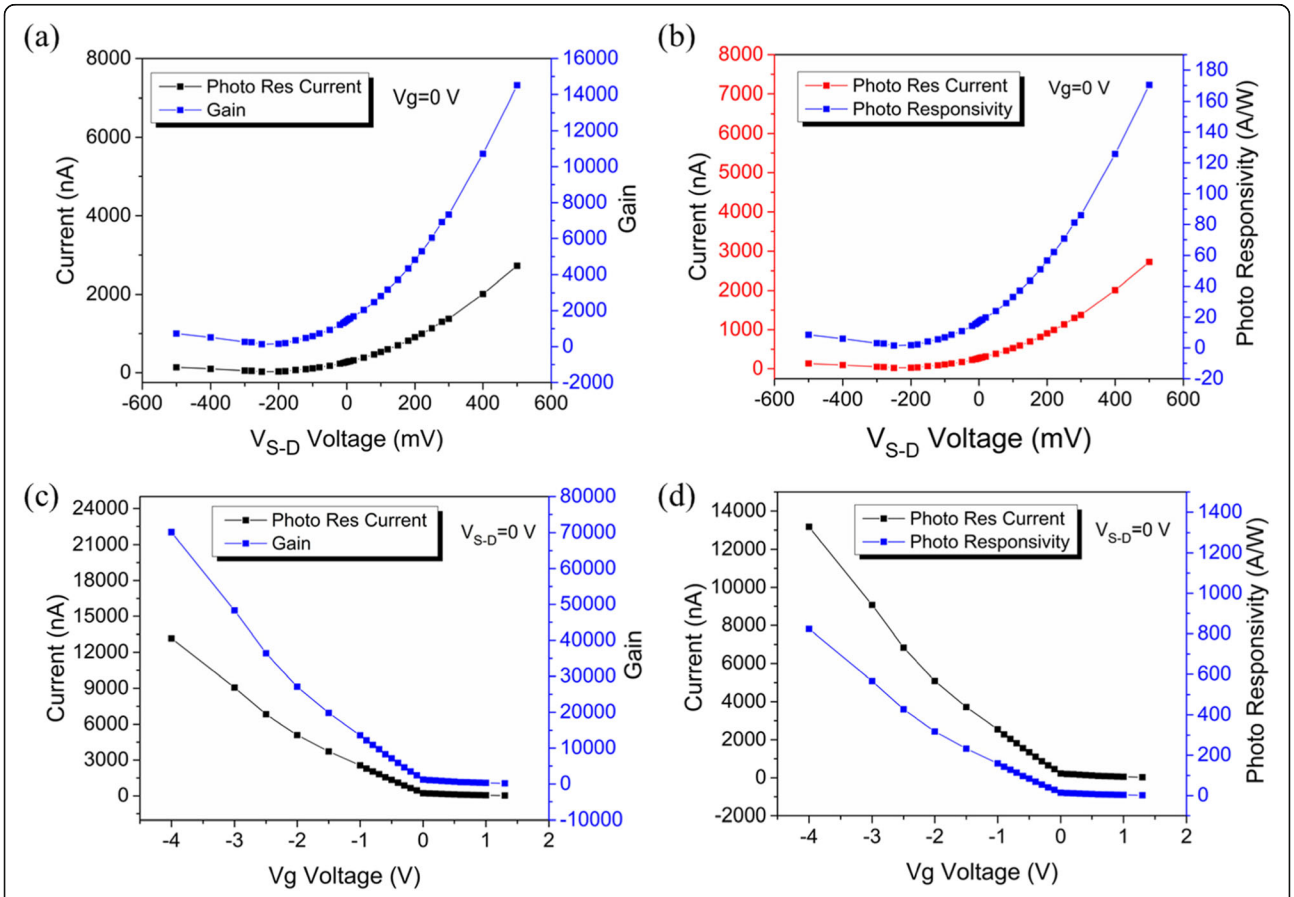

Fig. 4 Photoresponsivity dependence on the biased source-drain voltage and gate voltage. **a** and **b** reveal the source-drain voltage dependence of photoresponsivity and gain, respectively, **c** and **d** show the back-gate voltage dependence of photoresponsivity and gain, respectively

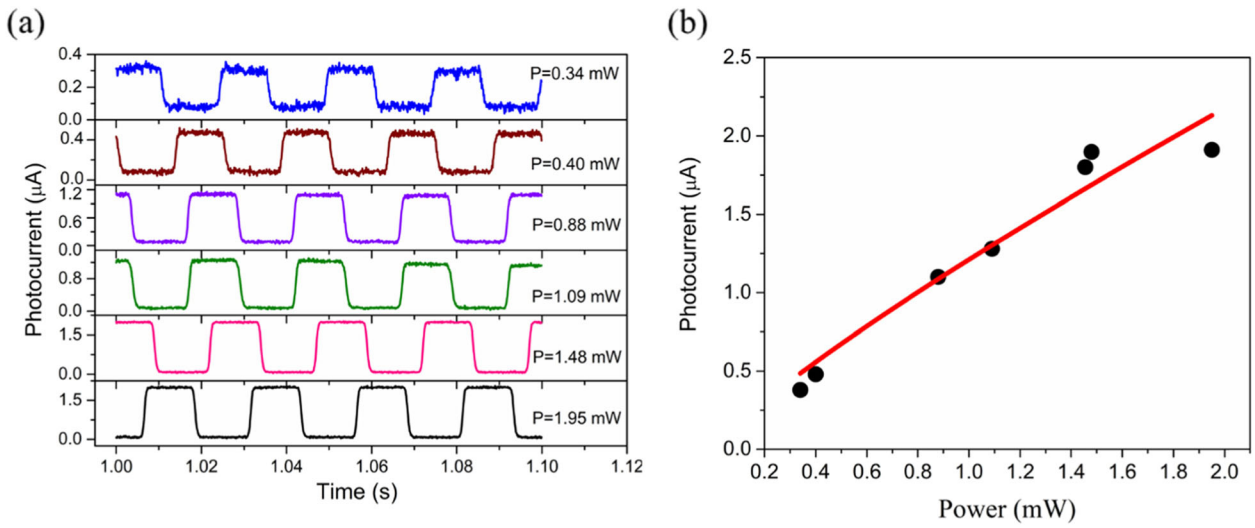

Fig. 5 **a** The time-dependence photocurrent measurements under the different power of incident light. **b** The power dependence of the photocurrent's properties. The results indicate that the GRN photodetector possessed a high photosensitivity property achieving mW-level input optical power detection

electrons were captured during the transition from the valence band to the conduction band by the midgap states [33] induced by the edge defects of GNRs. Therefore, before the holes and the trapped electrons recombined, the holes could circulate between the drain-source electrodes to form the photocurrent, achieving a high gain. The third aspect was that the accumulation of electrons at the SiO_2/Si interface was equivalent to applying a vertical electric field, and thus the conductance of the channel was greatly enhanced. Furthermore, in Fig. 2a–d, the obtained photocurrent had little dependence on the frequency of incident light modulated by an optical chopper, which is similar to the reported MoS_2 photodetector [24]. The photoconductive effect played the primary role in the photocurrent generation of the GNR photodetector when the frequency of light was regulated by the chopper. However, when the device was exposed to light (0 Hz), the photogating effect would be significant in the process of carriers generation, leading to trapping and recombination within semiconductors.

The detailed physical process of the third aspect discussed above was demonstrated in Fig. 2e, f. To achieve an equilibrium state in the dark, electrons would diffuse from SiO_2 to Si due to the difference of Fermi levels between the two materials, which led to energy band bending at the Si/SiO_2 interface. As a result, a strong built-in electric field (E) was formed in the depletion region, which efficiently separated the photogenerated electron-hole pairs with the electrons moving to the interface between Si and SiO_2 while the holes transfering to the interior region of Si. The electrons then accumulated at the SiO_2/Si interface, and these trapped electrons applied an additional negative vertical voltage to the GNRs, where the presence of these electrons increased the hole concentration and lowered the Fermi level of the GNR channel accordingly.

Although the device displays high performance, it is of importance to seek several effective approaches to significantly boost the photocurrent and the responsivity of the device. Then, the effects of the source-drain bias and gate voltage on photocurrent were systematically investigated. Figure 3a shows results of photocurrent (I_{laser}), background current (I_{dark}), and photoresponse current (I_{ph}) measurements as a function of the source-drain voltage ($-3\ V \le V_{S-D} \le 10\ V$) at a fixed gate voltage. The photocurrent was not zero at $V_{S-D} = 0$ and increased nonlinearly with the source-drain voltage, also proving the existence of a built-in electric field. It is clear that the value of the photocurrent was strongly dependent on the source-drain bias.

A convincing explanation for the tunability via source-drain voltage is that the relationship between photocurrent, background current, and photoresponse current can be expressed as $I_{illumination} = I_{ph} + I_{dark}$, where I_{ph} and I_{dark} increased with drain-source voltage V_{S-D} because the drift velocity of carriers rised and the carrier transit time reduced under an external electric field [34]. Therefore, the separation efficiency of photogenerated carriers improved, significantly contributing to the large photocurrent. Such phenomenon indicates that the total electric field of the GNR channel, the sum of the internal electric field and the external electric field, can be modulated by V_{S-D}.

Moreover, considering the gate-tuneable carrier density of GNR, the photocurrent of our device was adjusted effectively by modulating the back-gate voltage. Figure 3b displays these three kinds of currents ($I_{illumination}$, I_{ph}

and I_{dark}) as a function of the back-gate voltage (− 5 V ≤ V_G ≤ 5 V) at V_{S-D} = 0. In general, the photocurrent was positively correlated with the absolute value of the gate voltage, because the carrier density of GNR was sensitive to the external vertical electric field. Interestingly, the photocurrent increased as the gate voltage increased when the gate voltage was negative (− 5 V ≤V_G ≤ 0 V), and the opposite occured when the gate voltage was positive (0 V ≤V_G ≤ 5 V). This phenomenon could be explained by the p-type behavior of the GNR channel, which agreeed well with the observation in Fig. 2d. The results indicate that the increased |V_G| can tune the Fermi level of the channel closer to the valence band (or conduction band) and the conductance of the GNR channel was gate-tuneable. Notably, for both the two modulation methods (source-drain voltage and back-gate voltage), the tunability of the photocurrent was demonstrated in an ultrawide range from nA-level to μA-level.

Additionally, the responsivity and gain could also be modulated efficiently by regulating the gate voltage and the source-drain voltage of the GNR photodetector. The gain and photoresponsivity dependence of the source-drain bias were calculated [according to Eqs. (1) and (2)] and subsequently plotted in Fig. 4a, b. For the photodetector based on GNRs, the relationship between the gain and V_{S-D} is given by the following formula:

$$G = \frac{\tau}{\tau_T} = \frac{\tau}{l^2/(\mu V_{S-D})} = \frac{\tau \mu V_{S-D}}{l^2} \quad (3)$$

where τ is excess hole lifetime (trapped hole lifetime), and $\tau_T = l^2/(\mu V_{S-D})$ is the transit time of the carrier, while l is the length of the channel and μ is the carrier mobility, whereas V_{S-D} is the source-drain bias. Hence, the gain and source-drain voltage exhibit a positive correlation. Apparently, G is linearly dependent on the source-drain bias. As a result, the maximum photoresponsivity of R = 170 AW^{-1} and the maximum gain of G = 14,500 were achieved at room temperature at V_{S-D} = 0.5 V, which was a 100-fold improvement over previous graphene-nanostructure-based photodetectors [26, 35, 36]. More importantly, the values of gain and photoresponsivity were not saturated. Consequently, a higher gain and photoresponsivity could be achieved if a larger drain-source voltage was applied.

Figure 4c, d shows that the photoresponsivity and gain could also be enhanced by applying a back-gate bias to improve the carrier concentration of the GNRs. The maximum photoresponsivity of R = 800 AW^{-1} and the maximum gain of G = 22400 were obtained at V_G = - 4 V. This maximum value of photoresponsivity was five orders of magnitude higher than that of pure graphene photodetectors (~ 10 mAW^{-1}) [37]. Furthermore, both gain and photoresponsivity were not saturated, therefore, a higher photoresponsivity could be achieved by applying a larger back-gate voltage. Besides the carrier concentration, another factor that significantly influenced the channel current was the contact resistance (R_C) between the Au electrodes and the GNRs which was inseparably related to the Schottky barrier height at the interface [34]. As the GNRs served as a p-type channel, when applying a negative V_G, the Schottky barrier height was reduced due to the lower Fermi level. In contrast, when the V_G was increased to a positive value, the Schottky barrier height was enhanced, and the current in the channel was greatly suppressed.

Finally, we turn to the time-dependence investigation of photocurrent under incident light of power. Figure 5a displays time-dependent photocurrent measurements under the different powers of incident light. This photocurrent was large enough for direct measurement without any current preamplifiers or lock-in amplifiers, even at an mW-level optical power. Figure 5b plots the photocurrent as a function of incident optical power. The photocurrent had a nonlinear relationship with incident power (I_{ph} = P^{α}, α = 0.85). Under lower light power, the contribution of the photogate current was dominant, and the photoconductive effect could be ignored due to a decrease in the number of photogenerated carriers [23]. Upon higher light illumination, on the contrary, an increasing current was observed, which could be attributed to the increased number of photogenerated electrons (photoconductive effect). Moreover, the device was sensitive to the incident light and the resulted photocurrent was closely related to the incident light energy, revealing the tremendous potential for optical power monitor. A comparison of optoelectronic parameters in various photodetectors is provided in Table 1.

Table 1 Comparison of critical performance indicators in photodetector based on 2D materials

Materials	Responsivity(A/W)	Response time(μs)	λ(nm)	Ref.
Graphene nanoribbons	800	10	532	This work
Graphene	32	150	532	[38]
Graphene nanoribbons	1.75	$> 2 \times 10^6$	1470	[39]
1 L MoS_2	7.5×10^{-3}	5×10^4	400–1000	[40]
1 L $MoSe_2$	97.1	1.5×10^5	532	[28]
1 L WS_2	9.2×10^{-5}	5.3×10^3	Visible	[41]

Conclusions

In summary, we have demonstrated a high-performance graphene nanoribbon photodetector modulated in a wide range through the external electrical field at room temperature. Meanwhile, without the external electric field, the performance of the device could be enhanced by the localized field at the Si/SiO_2 interface. The device exhibited a high photoresponsivity of 800 AW^{-1} at V_G = − 4 V, which was two orders of magnitude higher than those in the previous research. Furthermore, the structure of our device is much simpler compared to the previous graphene-based optoelectronic device with the potential broad applications. The performance of the graphene nanoribbon device can be further improved by h-BN encapsulation, surface plasmons, ferroelectric field, and hybrid structures. The proposed graphene nanoribbons photodetector opens up exciting opportunities for ultrafast and high sensitivity for future graphene-based safety monitoring, photo-communication, and aviation applications.

Acknowledgements

Y.P.L. would like to acknowledge Qijie Wang and Wen Siang Lew for useful discussions. This work was supported by Natural Science Foundation of China (grant no. 61775241), and partially funded by the Hunan Province Key Research and Development Project (grant no. 2019GK2233), Youth Innovation Team (grant no. 2019012) of Central South University, and the Science Project of State Key Laboratory of High-Performance Complex Manufacturing, Central South University (no. ZZYJKT2020-12), and Technology Innovation Basic Research Project of Shenzhen (grant no. JCYJ20180307151237242), and the Fundamental Research Funds for the Central Universities of Central South University (no.1053320182462). Z.W.L Z. L. acknowledges the funding support from the Australian Research Council (ARC Discovery Project, DP180102976).

Authors' Contributions

Y.P.L. and Z.W.L contributed to the experimental idea. J.Y prepared the graphene samples. J.H.Z. fabricated the device. Y.P.L, J.H.Z., and J.Y carried out experimental measurements and analysis of the experimental data. All authors contributed to discussions and manuscript revision. J.Y, J.H.Z, and X.F.K contributed equally to this work. All authors read and approved the final manuscript.

Competing interests

The authors declare that they have no competing interests.

Author details

[1]School of Electronics and Information, Hangzhou Dianzi University, 1158 Second Street, Xiasha College Park, Hangzhou 310018, Zhejiang, People's Republic of China. [2]School of Physics and Electronics, Hunan Key Laboratory for Super-microstructure and Ultrafast Process, Central South University, 932 South Lushan Road, Changsha, Hunan 410083, People's Republic of China. [3]State Key Laboratory of High-Performance Complex Manufacturing, Central South University, 932 South Lushan Road, Changsha, Hunan 410083, People's Republic of China. [4]Shenzhen Research Institute of Central South University, A510a, Virtual University Building, Southern District, High-tech Industrial Park, Shenzhen 518057, People's Republic of China. [5]School of Chemical and Biomolecular Engineering, The University of Sydney, Camperdown, Sydney, NSW 2006, Australia.

Received: 20 January 2020 Accepted: 11 May 2020
Published online: 03 June 2020

References

1. Cseri L, Baugh J, Alabi A, AlHajaj A, Zou L, Dryfe RAW et al (2018) Graphene oxide–polybenzimidazolium nanocomposite anion exchange membranes for electrodialysis. J Mater Chem A 6(48):24728–24739
2. Wu K, Yang H, Jia L, Pan Y, Hao Y, Zhang K et al (2019) Smart construction of 3D N-doped graphene honeycombs with (NH4)2SO4 as a multifunctional template for Li-ion battery anode: "A choice that serves three purposes". Green Chem 21(6):1472–1483
3. Fei F, Cseri L, Szekely G, Blanford CF (2018) Robust Covalently Cross-linked Polybenzimidazole/Graphene Oxide Membranes for High-Flux Organic Solvent Nanofiltration. ACS Appl Mater Interfaces 10(18):16140–16147
4. Feizi Mohazzab B, Jaleh B, Issaabadi Z, Nasrollahzadeh M, Varma RS (2019) Stainless steel mesh-GO/Pd NPs: catalytic applications of Suzuki–Miyaura and Stille coupling reactions in eco-friendly media. Green Chem 21(12): 3319–3327
5. Vallés C, Zhang X, Cao J, Lin F, Young RJ, Lombardo A et al (2019) Graphene/Polyelectrolyte Layer-by-Layer Coatings for Electromagnetic Interference Shielding. ACS Applied Nano Materials 2(8):5272–5281
6. Novoselov KS, Geim AK, Morozov SV, Jiang D, Zhang Y, Dubonos SV et al (2004) Electric Field Effect in Atomically Thin Carbon Films. Science. 306(5696):666
7. Geim AK, Novoselov KS (2007) The rise of graphene. Nat Mater 6(3):183–191
8. Bonaccorso F, Sun Z, Hasan T, Ferrari AC (2010) Graphene photonics and optoelectronics. Nat Photonics 4(9):611–622
9. Bao Q, Loh KP (2012) Graphene Photonics, Plasmonics, and Broadband Optoelectronic Devices. ACS Nano 6(5):3677–3694
10. Bolotin KI, Sikes KJ, Jiang Z, Klima M, Fudenberg G, Hone J et al (2008) Ultrahigh electron mobility in suspended graphene. Solid State Commun 146(9):351–355
11. Du X, Skachko I, Barker A, Andrei EY (2008) Approaching ballistic transport in suspended graphene. Nat Nanotechnol 3(8):491–495
12. Meric I, Han MY, Young AF, Ozyilmaz B, Kim P, Shepard KL (2008) Current saturation in zero-bandgap, top-gated graphene field-effect transistors. Nat Nanotechnol 3(11):654–659
13. Geim AK (2009) Graphene: Status and Prospects. Science. 324(5934):1530
14. Terrones M, Botello-Méndez AR, Campos-Delgado J, López-Urías F, Vega-Cantú YI, Rodríguez-Macías FJ et al (2010) Graphene and graphite nanoribbons: Morphology, properties, synthesis, defects and applications. Nano Today 5(4):351–372
15. Vakil A, Engheta N (2011) Transformation Optics Using Graphene. Science. 332(6035):1291
16. Avouris P (2010) Graphene: Electronic and Photonic Properties and Devices. Nano Lett 10(11):4285–4294
17. Ponraj JS, Xu Z-Q, Dhanabalan SC, Mu H, Wang Y, Yuan J et al (2016) Photonics and optoelectronics of two-dimensional materials beyond graphene. Nanotechnology. 27(46):462001
18. Zhou H, Gu T, McMillan JF, Yu M, Lo G, Kwong D-L et al (2016) Enhanced photoresponsivity in graphene-silicon slow-light photonic crystal waveguides. Appl Phys Lett 108(11):111106
19. Nair RR, Blake P, Grigorenko AN, Novoselov KS, Booth TJ, Stauber T et al (2008) Fine Structure Constant Defines Visual Transparency of Graphene. Science. 320(5881):1308
20. George PA, Strait J, Dawlaty J, Shivaraman S, Chandrashekhar M, Rana F et al (2008) Ultrafast Optical-Pump Terahertz-Probe Spectroscopy of the Carrier Relaxation and Recombination Dynamics in Epitaxial Graphene. Nano Lett 8(12):4248–4251
21. Tielrooij KJ, Song JCW, Jensen SA, Centeno A, Pesquera A, Zurutuza Elorza A et al (2013) Photoexcitation cascade and multiple hot-carrier generation in graphene. Nat Phys 9(4):248–252
22. Fang H, Hu W (2017) Photogating in Low Dimensional Photodetectors. Advanced Science 4(12):1700323
23. Gonzalez-Medina JM, Marin EG, Toral-Lopez A, Ruiz FG, Godoy A, editors. Numerical Investigation of the Photogating Effect in MoTe2 Photodetectors. 2019 International Conference on Simulation of Semiconductor Processes and Devices (SISPAD); 2019 4-6 Sept. 2019.
24. Furchi MM, Polyushkin DK, Pospischil A, Mueller T (2014) Mechanisms of Photoconductivity in Atomically Thin MoS2. Nano Lett 14(11):6165–6170

25. Konstantatos G, Badioli M, Gaudreau L, Osmond J, Bernechea M, de Arquer FPG et al (2012) Hybrid graphene–quantum dot phototransistors with ultrahigh gain. Nat Nanotechnol 7(6):363–368
26. Liu C-H, Chang Y-C, Norris TB, Zhong Z (2014) Graphene photodetectors with ultra-broadband and high responsivity at room temperature. Nat Nanotechnol 9(4):273–278
27. Cuevas A, Macdonald D (2004) Measuring and interpreting the lifetime of silicon wafers. Sol Energy 76(1):255–262
28. Abderrahmane A, Ko PJ, Thu TV, Ishizawa S, Takamura T, Sandhu A (2014) High photosensitivity few-layered MoSe2 back-gated field-effect phototransistors. Nanotechnology. 25(36):365202
29. Kwon J, Hong YK, Han G, Omkaram I, Choi W, Kim S et al (2015) Giant Photoamplification in Indirect-Bandgap Multilayer MoS2 Phototransistors with Local Bottom-Gate Structures. Adv Mater 27(13):2224–2230
30. Jo S-H, Park H-Y, Kang D-H, Shim J, Jeon J, Choi S et al (2016) Broad Detection Range Rhenium Diselenide Photodetector Enhanced by (3-Aminopropyl)Triethoxysilane and Triphenylphosphine Treatment. Adv Mater 28(31):6711–6718
31. Yin L, Zhan X, Xu K, Wang F, Wang Z, Huang Y et al (2016) Ultrahigh sensitive MoTe2 phototransistors driven by carrier tunneling. Appl Phys Lett 108(4):043503
32. Buscema M, Island JO, Groenendijk DJ, Blanter SI, Steele GA, van der Zant HSJ et al (2015) Photocurrent generation with two-dimensional van der Waals semiconductors. Chem Soc Rev 44(11):3691–3718
33. Winzer T, Knorr A, Malic E (2010) Carrier multiplication in graphene. Nano Lett 10(12):4839–4843
34. Lopez-Sanchez O, Lembke D, Kayci M, Radenovic A, Kis A (2013) Ultrasensitive photodetectors based on monolayer MoS2. Nat Nanotechnol 8(7):497–501
35. An X, Liu F, Jung YJ, Kar S (2013) Tunable graphene–silicon heterojunctions for ultrasensitive photodetection. Nano Lett 13(3):909–916
36. Yu WJ, Liu Y, Zhou H, Yin A, Li Z, Huang Y et al (2013) Highly efficient gate-tunable photocurrent generation in vertical heterostructures of layered materials. Nat Nanotechnol 8(12):952–958
37. Mueller T, Xia F, Avouris P (2010) Graphene photodetectors for high-speed optical communications. Nat Photonics 4(5):297–301
38. Liu Y, Xia Q, He J, Liu Z (2017) Direct observation of high photoresponsivity in pure graphene photodetectors. Nanoscale Res Lett 12(1):93
39. Yu X, Dong Z, Liu Y, Liu T, Tao J, Zeng Y et al (2016) A high performance, visible to mid-infrared photodetector based on graphene nanoribbons passivated with HfO2. Nanoscale. 8(1):327–332
40. Yin Z, Li H, Li H, Jiang L, Shi Y, Sun Y et al (2012) Single-layer MoS2 phototransistors. ACS Nano 6(1):74–80
41. Perea-López N, Elías AL, Berkdemir A, Castro-Beltran A, Gutiérrez HR, Feng S et al (2013) Photosensor Device Based on Few-Layered WS2 Films. Adv Funct Mater 23(44):5511–5517

Publisher's Note